RSC Advances

PAPER

View Article Online
View Journal | View Issue

Cite this: *RSC Adv.*, 2015, **5**, 3807

Comprehensive studies of pharmacokinetics and biodistribution of indocyanine green and liposomal indocyanine green by multispectral optoacoustic tomography†

Wantong Song,[a] Zhaohui Tang,*[a] Dawei Zhang,[a] Neal Burton,[b] Wouter Driessen[b] and Xuesi Chen*[a]

Received 3rd September 2014
Accepted 5th December 2014

DOI: 10.1039/c4ra09735a

www.rsc.org/advances

Real-time and continuous monitoring of systemically administered agents is an important task in pharmaceutical development. Herein, we performed a real-time continuous study of the pharmacokinetics and biodistribution of indocyanine green (ICG) and liposomal indocyanine green (Lipo-ICG) *in vivo* by multispectral optoacoustic tomography (MSOT). By comparing the blood clearance and uptake behavior of these two ICG formulations in liver, spleen, kidney and tumor, we showed that Lipo-ICG prolonged the retention time of ICG in blood, and resulted in enhanced accumulation and retention in liver, spleen, and tumor. The results obtained from the MSOT test provided a comprehensive and continuous view of the metabolic behavior of the injected agents in different formulations. The results may also be helpful for understanding this new imaging technique.

Introduction

Nanomedicines, drugs encapsulated in nanocarriers, have shown great potential in reducing the side-effects of chemotherapeutic drugs and improving the life quality of cancer patients.[1–3] Several nanomedicines, like doxorubicin encapsulated in pegylated liposomes (Doxil) and a polymeric micelle formulation of paclitaxel (Genexol-PM) have entered the market. Compared to free drugs, nano-drugs are characterized by long blood circulation time and distinct *in vivo* pharmacokinetic pathways. This has been extensively tested by sample collection and other imaging methods.[4–7] However, a continuous, real-time quantitative tracking of the agents after injection is still a challenge work.

The evaluation of biodistribution, and the pharmacokinetics thereof, constitutes important preliminary information when designing new drugs and contrast agents. In preclinical trials, the commonly applied method is to sacrifice mice at defined time points, collect plasma and tissue and measure the drug concentrations in each. By using a high number of replicates at each time point, the pharmacokinetic profiles in tissues of interest can be determined.[8,9] Alternatively, one can conjugate the drugs or drug carriers with fluorescent probes – commonly near infrared fluorescent dye – to enable noninvasive *in vivo* imaging of biodistribution. The *in vivo* pathway of the probes and the relative fluorescence intensities in each tissue reflect the behavior of the injected agents, and one can directly observe the fate of the drugs administered.[10,11] However, the limitation of optical imaging is the low resolution at depth, due to the scattering of photons in biological tissues. Whole-mouse optical imaging generally results in surface-weighted information that does not accurately reveal deep-tissue activity.[12,13] Although new technologies, like diffuse optical tomography (DOT), which could probe centimeters into tissue are being developed, the imaging depth is achieved at the expense of poor spatial resolution – equal to about one-third of the imaging depth.[14,15] Besides, long image acquisition time in the range of tens of minutes is needed for tomographic optical imaging (like fluorescence molecular tomography, FMT) to produce quantitative results, which is unsuitable for capturing fast-changing signals and continuous dynamic results.[16]

Optoacoustic tomography, also referred to as photoacoustic tomography, is an emerging modality that brings significant promise to solve the obstacles encountered in pure optical imaging.[17,18] In optoacoustic imaging, the scattering of photons is overcome by making use of the optoacoustic effect: following absorption of light energy by a molecule, the absorbed energy can be dissipated either by the emission of a photon of lower energy and heat, or entirely as heat. In either case, the released heat produces a thermoelastic expansion around the molecule, which results in the generation of a pressure wave that can be

[a]*Key Laboratory of Polymer Ecomaterials, Changchun Institute of Applied Chemistry, Chinese Academy of Sciences, Changchun, 130022, P. R. China. E-mail: ztang@ciac.ac.cn; xschen@ciac.ac.cn; Fax: +86-431-85262116; Tel: +86-431-85262116*

[b]*iThera Medical, Zielstattstrasse 13, Munich, Germany*

† Electronic supplementary information (ESI) available: Videos of ICG and Lipo-ICG in liver, spleen, tumor, 3D images of ICG and Lipo-ICG in tumor. See DOI: 10.1039/c4ra09735a

detected by an ultrasound transducer.[19] The key benefit of this mode of detection is that acoustic scattering is about three orders of magnitude lower than optical scattering in tissue, allowing one to maintain high spatial resolution at depth.[20–22] In the implementation used herein, multispectral optoacoustic tomography (MSOT) could generate images specific for chromophores of interest.[23–25] By illuminating at multiple wavelengths and performing multispectral unmixing, the spatial distribution and concentration of individual absorbers in an animal could be detected.[26] Furthermore, by parallel detection using a multi-element ultrasound transducer array, and operating the laser at a high repetition rate, real-time characterization of the injected contrast agents in organs of interest could be achieved.[27] This makes MSOT a new tool for *in vivo* pharmacokinetics and biodistribution studies.

In this study, we prepared a liposomal indocyanine green (Lipo-ICG) formulation, and performed a continuous, real-time quantitative observation of the blood clearance and *in vivo* distribution of Lipo-ICG and free ICG by MSOT. Comparative studies of these two ICG formulations related with blood circulation, uptake and relative concentration in liver, spleen, kidney and tumor along with representative tomographic images were provided.

Experimental section

Materials

ICG and cholesterol were purchased from Alfa Aesar, egg yolk phosphatidylcholine (eggPC) was purchased from Doosan Biotech Co. Korea. Stearic acid (SA) was purchased from Sino-Pharma. Co. Ltd, and mPEG2k-OH was purchased from Sigma-Aldrich. mPEG2K stearate (mPEG2k-SA) was synthesized by the condensation of mPEG2k-OH and SA catalyzed by diisopropylcarbodiimide (DIC) and *N*,*N*-dimethylaminopyridine (DMAP) in dichloromethane (CH_2Cl_2).

Preparation of Lipo-ICG

Lipo-ICG was prepared by reverse phase evaporation method. In brief, 50 mg eggPC, 40 mg cholesterol, 5 mg mPEG2k-SA was dissolved in 5 mL CH_2Cl_2, 5 mg ICG was dissolved in 10 mL Milli-Q water. The two solutions were then mixed together, sonicated for 100 s, then the organic solvent was evaporated from the mixture by rotary evaporation, and an ivory emulsion was obtained. To remove the un-entrapped ICG, the dispersion was subjected five times to ultrafiltration (MWCO = 50 000, 10 000 rpm, 10 min). The final dispersion was passed through an extruder with polycarbonate membrane filters (450 nm pore size). Liposome diameter was determined by the particle size analyzer (ZetaPALS, Brookhaven Instruments Corporation). The spectra of ICG were measured by UV-Vis spectrophotometer (UV-2401PC, SHIMADZU).

Animal model

All animal experiments were performed in compliance with the Guidelines for the Care and Use of Research Animals established by the Jilin University Animal Studies Committee.

Female Balb/C nude mice were used for all the photoacoustic studies. For the pharmacokinetic study, healthy nude mice were used. For the biodistribution study, C26 tumor bearing mice was applied. C26 cells were implanted subcutaneously at the left abdomen at a density of 2.0×10^6 cells in 0.1 mL PBS, and the experiments were conducted after tumor grew to a volume about 400 mm^3, as measured with a caliper (tumor volume = $0.5 \times a \times b^2$, where a represents the major axis, and b represents the minor axis).

MSOT equipment

The MSOT equipment (inVision 128) was purchased from iThera Medical (Munich, Germany), and includes a total of 128 ultrasound transducer elements, each at 5 MHz, arranged in an array of 270 degrees. Illumination of the imaging plane is achieved with an OPO pumped Nd:YAG laser, which is tunable in 1 nm steps between 680 nm and 980 nm. The maximum energy of this laser is 120 mJ. This energy is delivered to a 5 cm^2 surface of the mouse, resulting in a fluence of 20–25 mJ cm^{-2}. As the energy of the laser can vary from pulse to pulse and also over wavelengths, the MSOT signal is normalized by an integrated emitted energy measurement. Imaging is performed at a maximum rate of 10 Hz, the firing rate of the laser. The tuning of the laser between wavelengths occurs in milliseconds; the speed of multispectral measurements is therefore limited by the number of wavelengths used as well as the number of sequential pulses that can be averaged at each wavelength. Both the transducer array and light fiber outputs are submerged in a water bath. Mice are anaesthetized with 2% isofluorane throughout the experiments, and placed in a horizontal position in a holder surrounded by a thin polyethylene membrane to prevent direct contact with water and allow acoustic coupling between mouse and transducer array. The light fibers and ultrasonic transducer array are in a fixed position for all data acquisitions, whereas the mouse can be translated through the imaging plane using a linear stage.

Phantom test

Cylindrical phantoms (provided with the MSOT equipment, operated following the instruction) were applied to test the linearity of the MSOT system as well as the relationship between concentration and MSOT signal. Different concentrations of ICG in distilled water were injected into the middle cavity of the phantom, and the phantom was placed in the MSOT equipment. Images of the phantoms were taken at three different positions near the middle of the phantom, and data acquisition was performed using 10 averages at 792 nm.

Blood clearance study of ICG and Lipo-ICG

Healthy female Balb/C nude mice (average body weight of 20 g) were used for the pharmacokinetic study. The cross section with the jugular vein near the neck was set as the imaging region for the blood clearance study. We continuously acquired images at the maximum rate of 10 frames per second at 792 nm (the absorption peak of ICG) to capture the rapid change in signal levels with maximum time resolution.

MSOT imaging was performed according to the following protocol:

(1) Mice were catheterized with a syringe needle in the tail vein, and then placed in the MSOT system.

(2) Scanning proceeded for 10 min to establish a baseline signal.

(3) ICG or Lipo-ICG was injected.

(4) Single wavelength imaging continuously for 20 min.

The mean pixel intensity (a.u.) in the region of interest (ROI, jugular vein) was recorded and exported.

The ICG concentration in the blood was calculated by the following formula: (formula 1)

$$[\mathrm{ICG}] = \frac{\mathrm{MPI} - \mathrm{BaselineMPI}}{\mathrm{Initial(Max)MPI} - \mathrm{BaselineMPI}} \times \frac{\text{Injection concentration} \times \text{volume of injection}}{\text{blood volume of mice} + \text{volume of injection}} \quad (1)$$

Here, MPI represents the mean pixel intensity, obtained from the MSOT results. The blood volume of the mice is 6% of body weight (for a 20 g weight mouse, the blood volume is 1.2 mL), the injection concentration of ICG is 0.925 mg mL^{-1}, volume of injection is 0.2 mL.

The pharmacokinetic parameters were calculated using a non-compartmental model by the Drug and Statistics (DAS) software (Mathematical Pharmacology Professional Committee, China).

Uptake study in liver, spleen, kidney and tumors

For biodistribution, 7 excitation wavelengths based on the maxima and minima in the absorption spectra of the imaging agents and/or tissue absorbers (680 nm, 715 nm, 730 nm, 760 nm, 792 nm, 850 nm, 900 nm) were measured. The cross sections of liver, spleen/kidney and the region of tumor were selected for scanning, with 5 frames averaged per wavelength. The experiment was performed following the protocol in 5.2. The metabolism of ICG was measured by scanning continuously for 2 h, and Lipo-ICG was scanned continuously for 3 h. For 3D reconstruction of the tumor region, the stage was advanced by 0.2 mm after each cycle of wavelengths was measured. After acquisition, the images were reconstructed using a backprojection algorithm, and linear spectral unmixing was applied as implemented in the ViewMSOT software (iThera Medical, Munich, Germany) to resolve signals of ICG from oxy- and deoxyhemoglobin (HbO_2 and Hb), which are the dominant absorbers in biological tissue.

Results

Preparation of Lipo-ICG

In order to capture the fast changing *in vivo* distribution of the injected contrast agents, we conducted a comprehensive study of ICG kinetics by the MSOT technique. ICG is an FDA approved cyanine dye that is used as an optical contrast agent in humans.[28] It has absorbance in the near-infrared region with a maximum absorption at 792 nm. To compare differential kinetics and biodistribution of non-encapsulated ICG *versus* a nanocarrier formulation, we prepared liposomal ICG (Lipo-ICG) by reverse phase evaporation, with mPEG2k-SA for prolonging the circulation time of the liposomes in blood (Fig. 1A). The mean size of the obtained Lipo-ICG was 196 ± 24 nm, with similar UV-Vis absorbance spectra to that of free ICG at the same concentration (Fig. 1B). To discriminate the injected chromophores from the intrinsic absorbers such as oxy- and deoxyhemoglobin (HbO_2 and Hb), the spectral signatures of Hb, HbO_2 and ICG between 680–900 nm were imported for multispectral processing (MSP, Fig. 1C). The functional dependency of the pixel intensities in MSOT and the ICG concentrations was conducted by phantom studies. As shown in Fig. 1D, the mean pixel intensity obtained from MSOT showed a clear correlation with the ICG concentration. Therefore, the MSOT measurements can provide the relative quantification of the imaging agents *in vivo*.

Pharmacokinetics of ICG and Lipo-ICG

We then measured the pharmacokinetics of ICG and Lipo-ICG in healthy Balb/C nude mice by MSOT. The imaging device used in this study contains a motorized stage that enables cross-sectional imaging throughout the longitudinal axis of the animal. By repeatedly scanning a single cross section, real-time changes in MSOT signals can be monitored *in vivo* at a maximum rate of 10 Hz, the repetition rate of the laser. The relative concentration change of the imaging agents in the region of interest (ROI) can be calculated according to the mean pixel intensity changes. Multispectral measurements enable determination of the change in concentration specific for a particular absorber. However, using multiple wavelengths comes at the cost of temporal resolution. In order to capture the fast signal changes in plasma, we performed the

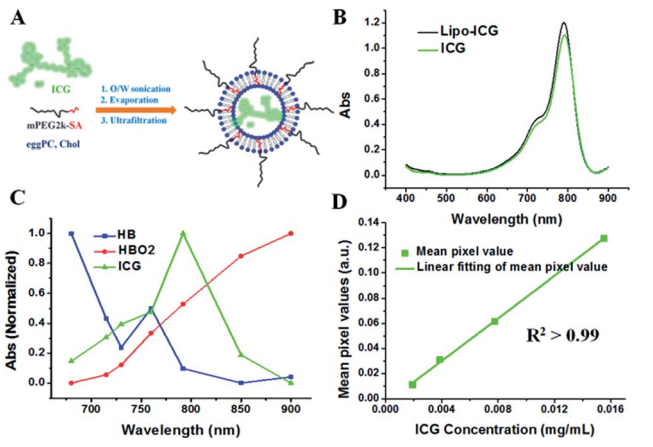

Fig. 1 Preparation and characterization of Lipo-ICG and ICG. (A) Preparation procedure of Lipo-ICG. (B) UV-Vis absorption spectra of ICG and Lipo-ICG in water from 400 nm to 900 nm, with the same maximum absorption at 792 nm. (C) The spectra of Hb, HbO_2 and ICG used for multispectral processing (seven wavelengths at 680 nm, 715 nm, 730 nm, 760 nm, 792 nm, 850 nm and 900 nm were utilized for determination of the spectra). (D) The photoacoustic signals are linearly dependent on the ICG concentrations.

pharmacokinetic experiments of ICG and Lipo-ICG at a single wavelength of 792 nm, by measuring the signal change in the jugular vein.

Single wavelength MSOT images at 900 nm provide the most clear tomographic anatomical information, since HbO_2 has increasing absorbance from 680 to 900 nm. The jugular vein was seen as a hyperintensity in grey scale image of the neck area of the mouse (red circle, Fig. 2A). Then ICG or Lipo-ICG was injected into different mice *via* the tail vein, and images were captured continuously at 792 nm for 20 min. Representative MSOT images (Fig. 2A, 792 nm, jet color scheme) reflected the signal changes that occurred in the jugular vein before and after ICG and Lipo-ICG administration, and indicated the ICG concentration changes in the blood. We then calculated the ICG concentration in blood according to formula 1, assuming that the circulating blood was 6% of mice weight.[29] The blood concentration–time profiles of ICG after intravenous injection are illustrated in Fig. 2B and the corresponding pharmacokinetic parameters are summarized in Table 1. As presented in Fig. 2B, the ICG concentration of Lipo-ICG in the blood stream was much higher than that of free ICG, even though the same dosage (9.25 mg kg^{-1}) was administered. Moreover, the AUC for Lipo-ICG was 1.6 times of that for ICG (815.5 *vs.* 527.3 μg mL^{-1} × min, Table 1). In comparison with free ICG, the liposome loading prolonged the half-life of ICG in blood ($T_{1/2}$) from 3.1 to 10.2 min. Additionally, the corresponding body clearance rate (CL_obs) decreased from 10.0 to 5.3 mL min^{-1} kg^{-1}. These results implied that the clearance of ICG from blood was decelerated by liposome loading, similar to that reported and tested in other methods.[30,31]

Table 1 Pharmacokinetic parameters of ICG and Lipo-ICG, calculated from the data obtained in the blood/jugular vein[a]

Parameter	ICG	Lipo-ICG	Unit
R^2	0.93	0.94	—
$T_{1/2}$	3.1	10.2	min
AUC_{all}	527.3	815.5	μg mL^{-1} × min
CL_obs	10.0	5.3	mL min^{-1} kg^{-1}

[a] R^2, R square. $T_{1/2}$ half-life of the drug. AUC_{all}, area under the drug concentration time curve. CL_obs, body clearance rate.

Uptake and distribution of ICG and Lipo-ICG in liver, spleen and tumor

The uptake behavior of ICG and Lipo-ICG in metabolic organs (liver, spleen, and kidney) were conducted on murine colon adenocarcinoma (C26) bearing Balb/C nude mice. Clear images at lung and heart were difficult to obtain because of the scattering of acoustic signal in the lung cavum. The distributions of these two ICG formulations in tumors were also investigated. Since signal changes in metabolic organs are much slower than that in plasma, multi-spectral processing (MSP) was applied here, by repeated scanning at seven wavelengths at 680 nm, 715 nm, 730 nm, 760 nm, 792 nm, 850 nm and 900 nm. Tomographic images of liver, spleen, kidney, and tumor were alternately obtained in the same mouse, and continuous scanning was conducted for 2 and 3 h for ICG and Lipo-ICG, respectively, using 5 average frames per wavelength.

Fig. 3 shows the time-resolved uptake behavior in liver after the same dosage (9.25 mg kg^{-1}) of ICG and Lipo-ICG

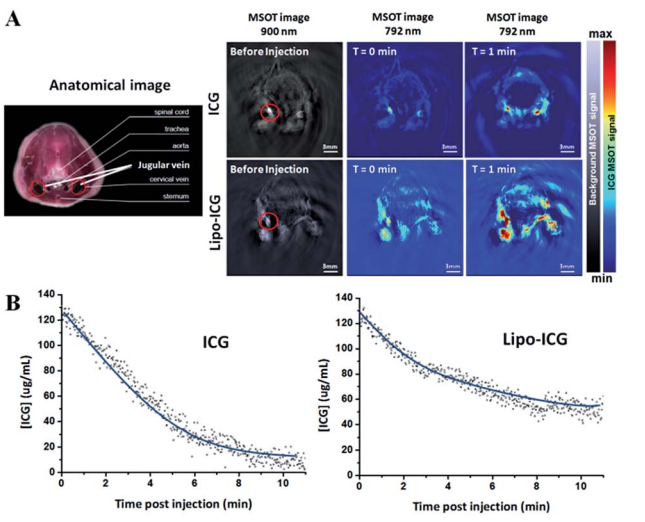

Fig. 2 Pharmacokinetics study of ICG and Lipo-ICG. (A) Anatomical images from the iThera software of the scan slice (RGB image), MSOT images at 900 nm before injection (grey), and MSOT images at 792 nm (jet) before and at 1 min after injection (scale bar = 3 mm). The left jugular vein was set as the region of interest (ROI), and outlined with a red circle. The test was performed by scanning at a single wavelength at 792 nm. (B) Plot of the ICG concentrations (converted from the mean ICG signal value inside the ROI) *vs.* time in 11 min post injection (blank dots) and the corresponding exponential decay fit (blue line).

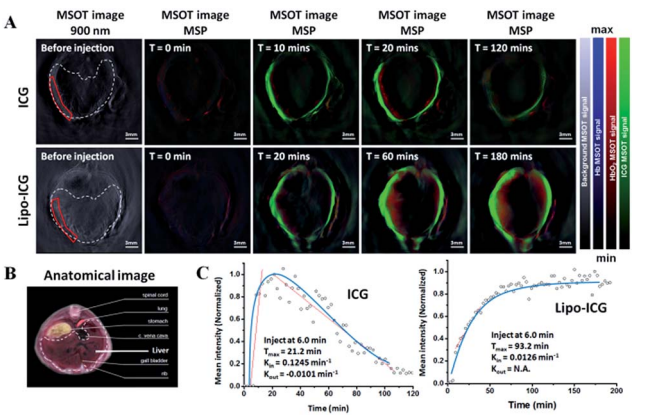

Fig. 3 Time-resolved uptake of ICG and Lipo-ICG in liver. (A) MSOT images of liver (outlined in white dashed lines) at 900 nm before injection (grey), time-resolved MSP images before and after injection (blue-Hb, red-HbO_2, green-ICG, scale bar = 3 mm). Regions of interest (ROI) were outlined in the red ellipse in the leftmost images. (B) Anatomical image of liver cross section from the iThera software (the liver region was outlined in white dashed line). (C) Temporal evolution of signal (circle dots, each normalized to their smoothed maxima) in the ROI. The inset contains the calculated values of the plot (blue line), T_{max} (time to reach the max intensity, interpolated from the raw data), K_{in} and K_{out} (uptake and clearance rate constant, calculated by determining the slope of the red lines, which was obtained from the linear fitting of the circle dots).

administration. The single wavelength MSOT images at 900 nm showed the tomographic anatomical information of liver. The stacked MSP images recorded the signal changes in the liver lobe before and after injection, with blue, red and green representing Hb, HbO_2 and ICG, respectively. Since the deposition in liver was high after ICG injection, clear excitation only happened at the periphery. To avoid well-characterized fluence-issues in highly absorbing tissue, especially after injection of contrast, regions-of-interest near the margin were chosen. The normalized mean pixel intensity–time profiles of ICG after intravenous injection were illustrated in Fig. 3C. After injection at 6 min, free ICG quickly concentrated in the liver, and reached a maximum at 21.2 min. Then, the imaging agents were quickly excreted from liver, and signals were almost undetectable within 2 h. The temporal behavior of Lipo-ICG in liver was completely different from that of free ICG. After injection at 6 min, Lipo-ICG showed a gradual accumulation in liver, with a maximum at 93.2 min, and remained static until the end of the observation interval at 3 h. The uptake rate constant K_{in} of Lipo-ICG was much smaller than that of free ICG (0.0126 min^{-1} *vs.* 0.1245 min^{-1}). This difference could be directly appreciated in the MSP tomographic images: free ICG quickly diffused into liver and cleared out in 2 h, while Lipo-ICG gradually accumulated in liver and maintained a high concentration until 3 h.

Fig. 4 provides the time-resolved uptake behavior of ICG and Lipo-ICG in spleen. Spleen and kidney could be observed within the same tomographic slice. However, no obvious ICG accumulation happened in kidney for ICG or Lipo-ICG, indicating that neither of these two formulations are cleared renally. The observations in spleen were similar to those in liver, with free ICG quickly diffusing into and out of the spleen, while Lipo-ICG gradually accumulated there. The normalized mean pixel intensity–time plots of ICG in spleen were also provided in Fig. 4C. After injection at 6 min, the maximum concentration of ICG in spleen appeared at 11.1 min, while 65.6 min for Lipo-ICG. Strong signal was maintained for Lipo-ICG in spleen for the duration of our observation period of 3 h.

Time-resolved diffusion and distributions of ICG and Lipo-ICG in C26 tumors were then studied by MSOT (Fig. 5). C26 tumors were implanted subcutaneously in the left abdomen of Balb/C nude mice, and the experiments were conducted when tumors reached a volume of about 400 mm^3. The tumor region was identified in the single wavelength MSOT images at 900 nm, and outlined by a red ellipse. In contrast to other optical methods which provide a planar surface image of the whole tumor, MSOT provides tomographic images which will uncover distribution information at depth. For free ICG, after injection at 6 min, an instant ICG diffusion happened near the surface vessels of the mouse (T = 10 min). However, similar to that happened in liver and spleen, the ICG signal quickly disappeared in 20 min, and almost can not be seen in 120 min. The lipo-ICG showed gradually accumulation and retention in tumor during the 3 h observation, which may be attributed to the prolonged retention time of Lipo-ICG in blood.

Last, the relative distribution of ICG and Lipo-ICG in these metabolic organs and tumors was examined by comparing the mean pixel intensities. As shown in Fig. 6, the main *in vivo* excretion pathway of free ICG was liver, while obvious retention of Lipo-ICG was observed in liver and spleen. Kidney is not a

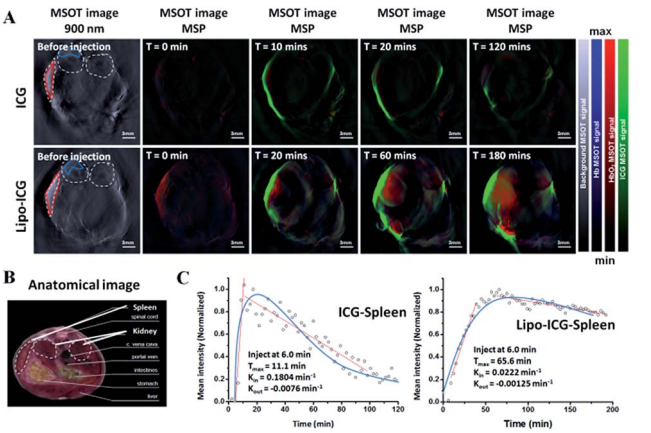

Fig. 4 Time-resolved uptake of ICG and Lipo-ICG in spleen. (A) MSOT images of spleen and kidney (outlined in white dashed lines) at 900 nm before injection (grey), time-resolved MSP images before and after injection (blue-Hb, red-HbO_2, green-ICG, scale bar = 3 mm). The regions of interest (ROI) for spleen and kidney were circled in red and blue, respectively. No obvious signal was seen in kidney, indicating that both ICG and Lipo-ICG were not cleared through kidney. (B) Anatomical image of spleen and kidney cross section from the iThera software (outlined in white dashed line). (C) Temporal evolution of signal (circle dots, each normalized to their smoothed maxima) in spleen. The inset contains the calculated values of the plot (blue line), T_{max} (time to reach the max intensity, interpolated from the raw data), K_{in} and K_{out} (uptake and clearance rate constant, calculated by determining the slope of the red lines, which was obtained from the linear fitting of the circle dots).

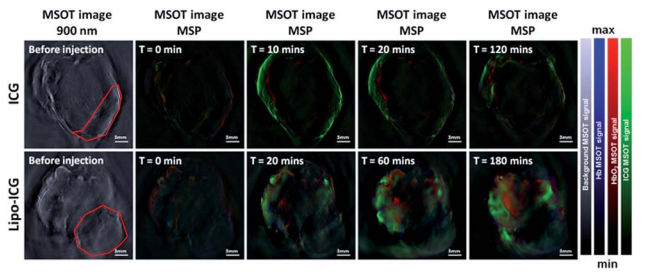

Fig. 5 Distribution of ICG and Lipo-ICG in C26 tumors. The tumor region was outlined in the red circle in the leftmost MSOT images at 900 nm (grey), scale bar = 3 mm.

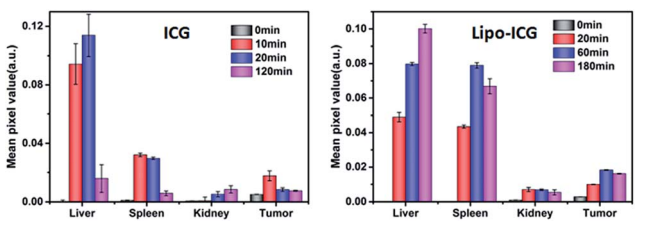

Fig. 6 Mean pixel values of ICG and Lipo-ICG in liver, spleen, kidney and tumor (n = 3).

central metabolic organ for neither of these two ICG formulations. The distributions of both ICG and Lipo-ICG were relatively low in tumors than in other organs. However, the Lipo-ICG formulation still showed enhanced accumulation and retention effect during our observation period.

Discussion

Photoacoustic imaging is a newly emerging technique for biomedical applications. It combines the advantages of optical and ultrasound imaging by penetrating deep into tissue with high spatial resolution, while maintaining the high contrast of optical imaging. In addition, due to the high repetition rate of the laser, and the ability to rapidly switch wavelengths, it is possible to acquire real-time *in vivo* information on the distribution of optical agents. In this study, we used the multispectral optoacoustic tomography (MSOT) technique to perform the real-time tracking of the blood clearance and tissue uptake process of ICG and Lipo-ICG, a small molecular imaging agent and its nanocarrier-loaded formulation. As seen in the MSOT images and plots, free ICG showed quick blood clearance and fast diffusion into liver and spleen, similar to other known small molecular agents. The loading of ICG in liposomes resulted in reduced clearance rate in blood, and gradual accumulation in liver, spleen, kidney and also tumors. Since high rate repeated scanning was conducted continuously for 2 or 3 h, real-time dynamic processes was obtained. The uptake and diffusion flashes of ICG and Lipo-ICG in liver, spleen and tumor section were provided in the (ESI,† S1-ICG-Liver, S2-ICG-Spleen, S3-ICG-Tumor. S4-Lipo-ICG-Liver, S5-Lipo-ICG-Spleen, S6-Lipo-ICG-Tumor).

Unlike other optical techniques which provide whole-body planar photonic images, MSOT uses tomography to obtain high resolution information throughout the cross section of the mouse. Organ information can be obtained by detecting the entire slice of interest. Planar optical imaging shows a bias towards surface information, and it is not possible to discriminate high signals at depth from weak signals at the surface. MSOT can provide detailed structures at depth and due to the use of tomography, signals at depth can be spatially discriminated. This is fascinating since the distribution in each organ is heterogeneous. Here, we pay our attention to the tumor region, since heterogeneity is a general feature of tumor tissue. As seen in the MSP images in Fig. 5, the diffusion of ICG mainly happened on the surface at the tumor region, while no obvious signal was detected in the interior. Since the overlying MSP images also provided the HbO_2 and Hb information (red and blue), the blood supply information on this section could be obtained simultaneously. Strong ICG signals were always observed at the position with strong HbO_2 signal, indicating that blood supply played an important role in drug diffusion. For the C26 tumor model applied here, the tumor region shows sparse signal compared to surrounding tissues, therefore, the drug diffusion in tumor was relatively low.

In the current study, a typical tomographic slice was applied to reflect the drug distribution behavior of the whole organ. This is likely to be more appropriate for the metabolic organs, because they are relatively homogenous tissues. However, a high level of heterogeneity is expected for the tumor region. To clarify this, we conducted a test on the whole tumor at the end of each MSOT test, by continuous scanning at a stepping size of 0.2 mm. Then the 3D image of the whole tumor was obtained by reconstructing the continuous tomographic images. These results are supplemented in the (ESI,† S7-ICG-Tumor-3D@2 h, S8-Lipo-ICG-Tumor-3D@3 h). The results also showed that Lipo-ICG would help agents accumulation in the tumors, especially near the tumor vessels at the margin.

Conclusions

A real-time continuous observation of the blood clearance and tissue uptake of ICG and Lipo-ICG was performed by MSOT. ICG quickly diffused in and out of liver and spleen, while Lipo-ICG showed a prolonged circulation time in blood, with gradual accumulation in liver and spleen. Optoacoustic images showed that the distribution in each organ was heterogeneous. The distributions and diffusion of both ICG and Lipo-ICG were vascular-dependent, with more agents appeared at the position with abundant vessels. Lipo-ICG showed enhanced accumulation and retention in tumors compared to free ICG. The results showed here provide a new insight into understanding the metabolic behavior of the nano-drug formulations.

Acknowledgements

This research was financially supported by National Natural Science Foundation of China (Projects 51173184, 51373168, 51021003, 51233004, 51321062, 51390484 and 51403204), Ministry of Science and Technology of China (International Cooperation and Communication Program 2011DFR51090), and the Program of Scientific Development of Jilin Province (20130206066GX, 20130727050YY).

Notes and references

1 D. L. Stirland, J. W. Nichols, S. Miura and Y. H. Bae, *J. Controlled Release*, 2013, **172**, 1045–1064.
2 Y. Matsumura and K. Kataoka, *Cancer Sci.*, 2009, **100**, 572–579.
3 S. Jokar, A. Pourjavadi and M. Adeli, *RSC Adv.*, 2014, **4**, 33001–33006.
4 T. Y. Kim, D. W. Kim, J. Y. Chung, S. G. Shin, S. C. Kim, D. S. Heo, N. K. Kim and Y. J. Bang, *Clin. Cancer Res.*, 2004, **10**, 3708–3716.
5 A. Gabizon and D. Papahadjopoulos, *Proc. Natl. Acad. Sci. U. S. A.*, 1988, **85**, 6949–6953.
6 A. Soundararajan, A. Bao, W. T. Phillips, R. Perez and B. A. Goins, *Nucl. Med. Biol.*, 2009, **36**, 515–524.
7 X. Sun, X. Huang, J. Guo, W. Zhu, Y. Ding, G. Niu, A. Wang, D. O. Kiesewetter, Z. L. Wang, S. Sun and X. Chen, *J. Am. Chem. Soc.*, 2014, **136**, 1706–1709.
8 H. Uchino, Y. Matsumura, T. Negishi, F. Koizumi, T. Hayashi, T. Honda, N. Nishiyama, K. Kataoka, S. Naito and T. Kakizoe, *Br. J. Cancer*, 2005, **93**, 678–687.

9 W. Song, Z. Tang, D. Zhang, Y. Zhang, H. Yu, M. Li, S. Lv, H. Sun, M. Deng and X. Chen, *Biomaterials*, 2014, **35**, 3005–3014.
10 R. Weissleder, C. H. Tung, U. Mahmood and A. Bogdanov, *Nat. Biotechnol.*, 1999, **17**, 375–378.
11 X. X. He, K. M. Wang and Z. Cheng, *Wiley Interdiscip. Rev.: Nanomed. Nanobiotechnol.*, 2010, **2**, 349–366.
12 V. Ntziachristos, J. Ripoll, L. H. V. Wang and R. Weissleder, *Nat. Biotechnol.*, 2005, **23**, 313–320.
13 J. G. Fujimoto, C. Pitris, S. A. Boppart and M. E. Brezinski, *Neoplasia*, 2000, **2**, 9–25.
14 J. P. Culver, V. Ntziachristos, M. J. Holboke and A. G. Yodh, *Opt. Lett.*, 2001, **26**, 701–703.
15 V. Ntziachristos, *Nat. Methods*, 2010, **7**, 603–614.
16 R. B. Schulz, A. Ale, A. Sarantopoulos, M. Freyer, E. Soehngen, M. Zientkowska and V. Ntziachristos, *IEEE Trans. Med. Imag.*, 2010, **29**, 465–473.
17 L. V. Wang, *Nat. Photonics*, 2009, **3**, 503–509.
18 L. H. V. Wang and S. Hu, *Science*, 2012, **335**, 1458–1462.
19 V. Ntziachristos and D. Razansky, *Chem. Rev.*, 2010, **110**, 2783–2794.
20 J. Levi, S. R. Kothapalli, S. Bohndiek, J. K. Yoon, A. Dragulescu-Andrasi, C. Nielsen, A. Tisma, S. Bodapati, G. Gowrishankar, X. R. Yan, C. Chan, D. Starcevic and S. S. Gambhir, *Clin. Cancer Res.*, 2013, **19**, 1494–1502.
21 A. de la Zerda, S. Bodapati, R. Teed, S. Y. May, S. M. Tabakman, Z. Liu, B. T. Khuri-Yakub, X. Y. Chen, H. J. Dai and S. S. Gambhir, *ACS Nano*, 2012, **6**, 4694–4701.
22 A. Hannah, G. Luke, K. Wilson, K. Homan and S. Emelianov, *ACS Nano*, 2014, **8**, 250–259.
23 J. Stritzker, L. Kirscher, M. Scadeng, N. C. Deliolanis, S. Morscher, P. Symvoulidis, K. Schaefer, Q. Zhang, L. Buckel, M. Hess, U. Donat, W. G. Bradley, V. Ntziachristos and A. A. Szalay, *Proc. Natl. Acad. Sci. U. S. A.*, 2013, **110**, 3316–3320.
24 N. Lozano, W. T. Al-Jamal, A. Taruttis, N. Beziere, N. C. Burton, J. Van den Bossche, M. Mazza, E. Herzog, V. Ntziachristos and K. Kostarelos, *J. Am. Chem. Soc.*, 2012, **134**, 13256–13258.
25 C. C. Bao, N. Beziere, P. del Pino, B. Pelaz, G. Estrada, F. R. Tian, V. Ntziachristos, J. M. de la Fuente and D. X. Cui, *Small*, 2013, **9**, 68–74.
26 J. Glatz, N. C. Deliolanis, A. Buehler, D. Razansky and V. Ntziachristos, *Opt. Express*, 2011, **19**, 3175–3184.
27 A. Taruttis, S. Morscher, N. C. Burton, D. Razansky and V. Ntziachristos, *PLoS One*, 2012, **7**, e30491.
28 D. B. Hunton, J. L. Bollman and H. N. Hoffman, *Gastroenterology*, 1960, **39**, 713–724.
29 L. Z. Zhang, Y. J. Zhang, W. Wu and X. Q. Jiang, *Chin. J. Polym. Sci.*, 2013, **31**, 778–786.
30 J. T. Alander, I. Kaartinen, A. Laakso, T. Pätilä, T. Spillmann, V. V. Tuchin, M. Venermo and P. Välisuo, *Int. J. Biomed. Imaging*, 2012, **2012**, 940585.
31 A. K. Kirchherr, A. Briel and K. Mader, *Mol. Pharmaceutics*, 2009, **6**, 480–491.